Large temperature range model for the atmospheric pressure chemical vapor deposition of silicon dioxide films on thermosensitive substrates

Konstantina Christina Topka[a,b], *George Alexander Chliavoras*[a], *François Senocq*[b], *Hugues Vergnes*[a], *Diane Samelor*[b], *Daniel Sadowski*[b], *Constantin Vahlas*[b], *Brigitte Caussat*[a,*]

[a] *Laboratoire de Génie Chimique (LGC), Université de Toulouse, CNRS, Toulouse, France*
[b] *Centre Interuniversitaire de Recherche et d'Ingénierie des Matériaux (CIRIMAT), Université de Toulouse, CNRS, Toulouse, France*

Coating complex surfaces by functional amorphous silica films for new applications including energy harvesting and health depends on the operating range and robustness of their deposition process. In this paper, we propose a new kinetic model for the atmospheric pressure chemical vapor deposition of SiO_2 films from $TEOS/O_2/O_3$ valid in the $150-520$ °C temperature range, thus allowing for treating thermally sensitive substrates. For this, we revisit reported chemical schemes in Computational Fluid Dynamics simulations considering original experimental data on the deposition rate of SiO_2 films from a hot-wall reactor. The new model takes into account for the first time a thermal dependency of the direct formation of SiO_2 from TEOS and O_3 and yields excellent agreement in both shape and value between experimental and calculated local deposition rate profiles. The model provides non-measurable information such as local distributions of species concentration and reaction rates, which are valuable for developing optimized CVD reactor designs. Original solutions for the introduction of the reactants are proposed, to uniformly coat complex and/or large parts at a wide temperature range.

1. Introduction

The chemical vapor deposition (CVD) of SiO_2 has been widely studied since thirty years (Kotani et al., 1989), mainly in semiconductor manufacturing as gate dielectrics (Inoue et al., 1987; Ding et al., 2001), and more recently in membrane-based gas separation and energy harvesting (Choi et al., 2013; Liang et al., 2019; Azizi et al., 2017). Other applications include the use of SiO_2 in optoelectronics, or as a component in antibacterial food packaging films (Varghese et al., 2013) and food safety monitoring sensors (Liu et al., 2016). Moreover, core@SiO_2–shell materials for solid phase extraction, catalyst support and SiO_2-nanocomposites used for wastewater treatment are receiving increasing attention (Zhang et al., 2011; Klaigaew et al., 2015; Zhang et al., 2019; Li et al., 2019). SiO_2 films are optically transparent, smooth and dense, acting as good insulation layers (Liu et al., 2019; Fonrodona et al., 2005) and corrosion barriers (Elam et al., 2017). The tetraethyl orthosilicate ($Si(OC_2H_5)_4$, TEOS)/ozone (O_3) thermal CVD processing route presents marked advantages compared to the other existing pathways using TEOS such as TEOS pyrolysis, particularly in the ability to treat thermally sensitive substrates at temperatures lower than 300 °C (Juárez et al., 2007; Okuyama et al., 1997). Films deposited by thermal CVD present excellent and tunable step coverage (Fujino, 1993; Yuan and Mokhtati, 1996; Levin, 1983), while hydrogen content and porosity are lower than in films processed by PECVD (Nagel et al., 2001),

improving as such the material's barrier and insulation properties. Furthermore, in comparison with the thermal TEOS/O_2 pathway, thermal TEOS/O_3 leads to higher deposition rates at lower operating temperatures, thanks to the reactivity of O_3 and the oxygen radicals generated through its thermal decomposition (Okuyama et al., 1997). The TEOS/O_3 route is therefore promising to treat complex-in-shape thermally sensitive substrates for innovative applications.

Succeeding in conformally coating complex substrates at low temperatures depends strongly on O_3 concentration (Shareef, 1995; Kawahara et al., 1992). The radicals produced by this chemistry are unstable, while the gas phase reactions are strongly dependent on temperature and radical species concentration (Shareef, 1996). Overcoming these drawbacks of the TEOS/O_3 route requires good control over the interplay between the transport phenomena, i.e. the local gas velocity, temperature and reactive species concentrations, as well as the homogeneous and heterogeneous chemical reactions leading to the formation of the film. As this interplay is difficult to establish experimentally, a valuable approach is to associate a targeted experimental investigation of the growth rates with reactor modelling. In particular, Computational Fluid Dynamics (CFD) codes can be used, in which appropriate chemical reactions and kinetic laws are implemented. In this perspective, the identification of the involved reactions and kinetics is often the bottleneck, since a wealth of unknown homogeneous and heterogeneous reactions occur simultaneously in CVD processes. A classical way to overcome this difficulty is to consider only apparent chemical reactions, meaning that each reaction represents, in a simplified way, many real chemical reactions that are otherwise difficult to determine in detail. The advantage of such an approach is the relative rapidity of development and the accuracy of the kinetic model, while the main drawback is that it is only valid for the operating range, in particular that of the deposition temperature for which it has been developed.

For the TEOS/O_3 CVD route, most of the relevant studies have been conducted in cold-wall low or atmospheric pressure CVD reactors using showerhead injectors (Schoof et al., 2002; Adachi et al., 2000; Fujimoto et al., 1999), such as the industrial Watkins Johnson reactors treating 200 mm silicon wafers, which were the main reactors of interest for the microelectronic industry in the nineties. Kim and Gill were among the first authors to study the TEOS/O_3 chemistry in a cold-wall reactor operating between 4 and 12 kPa, in a 280−405 °C temperature range (Kim, 1994). They developed a global apparent mechanism in which TEOS decomposes in the gas phase in the fictitious molecule "INT" and in ethanal, through an excited $O_3{}^*$ centered mechanism. This INT molecule represents the various unknown chemical species produced by the homogeneous decomposition of TEOS. It can be formed through the substitution of TEOS' ethoxy ligands by hydroxyl ligands, following the formula $Si(OH)_{n-1}(OC_2H_5)_{5-n}$, where n = 1–4 (Niéto, 2001). Additionally, INT can encompass oligomers, such as siloxane ones that are formed from the hydro-substitution of two intermediates with the previously mentioned formula (Satake et al., 1994; Sorita et al., 1993). A cascade of reactions resulting in the stepwise cleavage of the ethoxy ligands is also described (Romet et al., 2001). Once formed, the INT species can either contribute to SiO_2 deposition or decompose into parasitic gaseous by-products. Working between 400 and 425 °C and for a pressure range of 10^3–10^5 Pa, Dobkin et al. (1995) modified this model by assuming that deposition occurs due to the presence of oxygen radicals, and that both TEOS and the INT species contribute to film formation. Zhou et al. (1997) developed a new model based on the two previous ones for a Watkins Johnson reactor operating at atmospheric pressure between 500 and 550 °C. The main differences concern the assumption that TEOS must react with O_3 to form, in one hand, the INT species and gaseous unreactive molecules noted R, and on the other hand the SiO_2 film. The unreactive molecules R mentioned in the literature are CH_3CHO, EtOH, MeOH (Kawahara et al., 1992; Flores and Crowell, 2005; Arnó, 1999), while other authors assume the direct decomposition of such molecules into CO, CO_2 and H_2O (Dobkin et al., 1995; Zhou et al., 1997). Nieto et al. (2005) applied this model to the same type of reactor and adapted some kinetic constants to its specific chamber configuration. In particular, they decreased the kinetics of the deposition reaction from TEOS, and the conversion of INT species into parasitic by-products that do not contribute to the deposition. It is worth noting that for these studies, no thermal activation appears for the kinetics of the deposition from TEOS. Romet et al. (2001) improved the model of Dobkin et al. by considering up to 37 gas phase reactions, including the direct contribution of O_3 to intermediate species formation, gas phase oligomerization and formation of diols. Similarly to previous studies, they did not consider any temperature dependence of the deposition reactions, and additionally removed any direct contribution of TEOS to the formation of the SiO_2 film. However, their model failed to simulate the process above 400 °C at low TEOS flow rates.

In Watkins Johnson type reactors, the distance between the gas injector and the wafer is lower than 20 mm and the residence time of the gaseous reactive phase is short (<0.5 s), due to total flow rates exceeding 20,000 standard cubic centimeters per minute (sccm). Moreover, the wall and substrate temperature ranges are spanning mainly between 400 and 550 °C. It is thus inappropriate to use the developed chemical reactions and associated kinetic laws for significantly different configurations, in particular in reactors involving higher residence times and/or lower deposition temperatures, as we will present in the following sections.

The present work aims to develop a kinetic model for the atmospheric pressure CVD of SiO_2 from TEOS, O_2 and O_3 mixtures, with a larger range of validity in terms of substrate temperature and residence time, more suited to CVD reactor geometries and deposition parameters able to treat large and/or complex-in-shape substrates. We apply a methodology combining experimental studies and process analysis by CFD simulation, in order to bring new information on the chemical and kinetic phenomena governing the deposition. In that which follows, the experimental and the computational details will be introduced first. Then, the experimental thermal profiles and associated deposition rates will be presented and discussed. These results will first be simulated using existing literature models. The aim is to reveal discrepancies, which will serve to develop a novel kinetic scheme. Finally, the elaborated kinetic model will be validated by comparison with the experimental information, and the simulation results will be discussed prior to providing concluding remarks.

2.   Materials and methods

2.1.   Experimental process

CVD of SiO_2 films was performed in a horizontal, tubular, hot-wall reactor, schematically illustrated in Fig. 1a. The reactor consists of a fused silica tube with an inner diameter of 46 mm and a length of 700 mm, heated by a semitransparent furnace (Trans Temp, Thermcraft Inc.). The wall's temperature profile was measured every 20 mm along the tube under a N_2 gas flow of 4036 sccm using a type-K thermocouple with an accuracy of ±2 °C. Deposition experiments were performed at four different set point (SP) temperatures, namely 400, 450, 500 and 550 °C, defined as the temperature measured at 360 mm from the inlet, after which a 140 mm long isothermal region exists. The CVD reactor inlet is connected to three gas lines. A N_2 (99.9999%, Messer) dilution line with variable flow allows to fix the total gas flow at 4036 sccm for all runs and was heated at approximately 100 °C. A second line bubbled 89, 223 or 444 sccm of N_2 gas through a bubbler system containing TEOS (99.999%, Sigma–Aldrich), and transported the precursor's vapors towards the reactor. The bubbler was heated at 65.3 ± 0.1 °C, while the corresponding N_2 line was kept at approximately 85 °C to avoid recondensation of the precursor vapors. An O_2 (99.9995%, Messer) line passed 1960 sccm through an ozonator (Lab2b Laboratory Ozone Generator, Triogen LTD). The ozonator was operating at its maximum ozone production, providing an O_3 concentration of 60 mg/l at standard temperature and pressure, and thus supplying the reactor with an O_2/O_3 mixture. All three gas-lines were kept
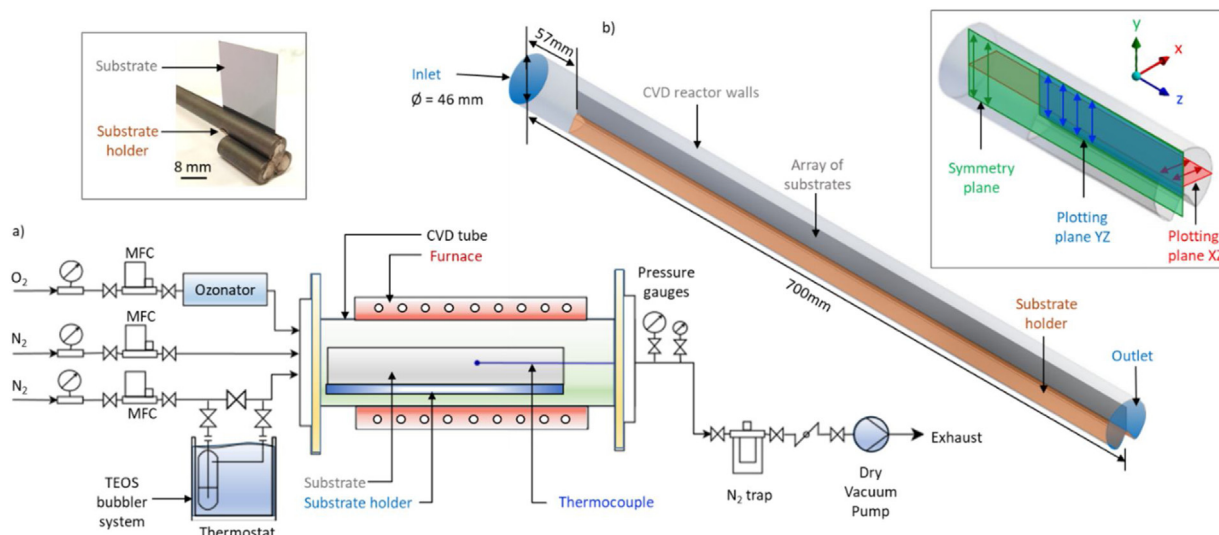
Fig. 1 – Schematic (a) and 3D (b) representation of the CVD reactor (not true-to-size and proportion). Top left inset photograph shows the substrate holder supporting a Si coupon vertically. Top right inset scheme depicts the symmetry plane, the plotting plane YZ used for surface results presentation and the plotting plane XZ used to present gas phase results.

separated, and their contents were mixed just at the inlet of the reactor. The system was always in excess of O_2. The reactor's base and operating pressures were monitored with a Pirani (MKS MicroPirani Transducer Series 925C) and a Baratron (MKS Baratron Type 627) gauges respectively, positioned downstream of the deposition zone, before a liquid nitrogen trap and a dry pump (Edwards, soXu 20iC). The operating pressure was fixed at 97.3 kPa (730 Torr) for all runs.

280 μm thick monocrystalline silicon (100) wafers (Neyco) were cut in rectangles of 32 $\times$ 24 mm^2 and used as substrates. Before being inserted into the reactor, the substrates were degreased in a succession of three ultrasound bath steps, including: (1) an ultrasound bath using distilled water for 5 min, then rinsed with acetone, (2) an ultrasound bath using acetone (>99%, VWR Chemicals) for 5 min, then rinsed with ethanol, (3) an ultrasound bath using ethanol (99.3%, VWR Chemicals) for 5 min, and finally dried under Ar (99.9999%, Messer) flow.

Within the reactor, the substrates were supported vertically by home-made, tubular, stainless steel substrate holders, with a 7 mm deep insertion slot, positioned on the row. Their total length was 450 mm, supporting a maximum of 18 coupons for each run. The first substrate was placed at a distance of 57 mm from the reactor inlet. Similar to Ponton et al.'s work (Ponton et al., 2018), the goal was to process SiO$_2$ films deliberately in a 360 mm long non-isothermal zone, existing before the *ca.*140 mm long isothermal zone, in order to obtain complementary mechanistic and kinetic information. Moreover, placing the first few substrates close to the reactor inlet allows addressing and quantifying the direct contribution of TEOS to the deposition, since the TEOS concentration is known only at the reactor inlet. Six runs were performed with a deposition duration ranging from 30 to 90 min, as summarized in Table 1.

Through experiments E1 to E3, the influence of the TEOS flow rate was evaluated for a SP temperature of 400 °C. Through runs E3–E6, the effect of the SP temperature was investigated, by fixing all flow rates.

2.2. Experimental validation

The average SiO$_2$ deposition rates were calculated from the deposited mass, by measuring each sample's weight differ-

ence before and after deposition using a Sartorius Genius Series ME215P analytical balance with 0.015 mg precision. For simplicity, it was assumed that deposition on each substrate surface is uniform. To convert the deposited mass to thickness and deposition rate, the films' density was taken equal to 2200 kg m^{-3} (Nieto et al., 2005). More accurate local thickness profiles were measured by reflective ellipsometry, using a Semilab SE-2000 ellipsometer operating in the $250-1000$ nm wavelength range. The incidence angle was kept constant at 70°. Each sample was probed in the center, 2 mm below the top edge, and the spectroscopic ellipsometry data were fitted in the $250-1000$ nm wavelength range using the software Semilab SEA. The Sellmeier model was utilized to extract the measured local thicknesses values. Fourier Transform Infra-Red (FTIR) spectroscopy measurements, detailed in Fig. S1 of *Supplementary material*, revealed that for all the conditions tested, the films are composed of pure SiO$_2$.

2.3. Process model

A CFD model considering gas phase and surface chemical reactions was developed to represent the reactive transport phenomena and the deposition rate taking place in the CVD reactor. The local gas flow and temperature profiles in the reactor were calculated by solving the mass and momentum conservation and thermal energy balance equations in each elementary discretized volume. The local distribution of species mass fractions and SiO$_2$ deposition rate were calculated after considering the kinetic data of the homogeneous and heterogeneous reactions into the species conservation equations. The implemented chemical reactions and kinetic laws were based on those developed by Zhou et al. (1997) and Nieto et al. (2005), as detailed below. The numerical simulations were run using ANSYS® FLUENT® 18.2, with a cell-centered finite volume scheme and second-order spatial accuracy. The assumptions considered to simplify the numerical complexity are the following:

- Steady state regime,
- Laminar gas flow (Reynolds number lower than 1000),

Table 1 – Deposition conditions of experimental runs performed in thermal CVD reactor.					
Run	SP T (°C)	N_2 flow rate through TEOS bubbler (sccm)	TEOS flow rate (sccm)	N_2 dilution flow rate (sccm)	Deposition time (min)
E1	400	444	10	1632	30
E2	400	223	5	1853	30
E3	400	89	2	1987	50
E4	450	89	2	1987	90
E5	500	89	2	1987	30
E6	550	89	2	1987	30

- Incompressible gas flow, due to the low value of the Mach number (<0.04) in the reactive zone,
- Heat of reactions neglected, due to high N_2 dilution,
- Ideal gases.

The physical properties of O_2, O_3, H_2O, CO, CH_3CHO and N_2 were taken from the FLUENT® database. They are calculated using the kinetic theory of gases and the Chapman-Enskog theory, as detailed in Bird et al. (2007), in which the Lennard Jones (LJ) parameters of these classical species are also given. The LJ parameters of the oxygen radical $O^{\bullet}$ (σ = 2.75 Å and ε/k = 80 K), and of TEOS (σ = 7.03 Å and ε/k = 522.7 K) were taken from the CHEMKIN database (Kee et al., 1998). Those of the intermediate (INT) were set equal to the parameters of TEOS. The molecular weight of INT was fixed at 180.27 g mol^{-1} by matching it to triethoxysilanol, $((Si(OH)(OC_2H_5)_3)$, one of the most probable intermediate species as reported by many authors (Kawahara et al., 1992; Romet et al., 2001; Flores and Crowell, 2005; Coltrin et al., 2000). All physical properties of the by-product produced by the INT were set equal to the latter.

The total reactive volume of the CVD reactor was represented by a three-dimensional (3D) geometrical domain (Fig. 1b) of 1,927,954 hexahedral and tetrahedral cells. Due to symmetry along the YZ plane (top right inset scheme of Fig. 1) and in order to reduce the computational time, only half of the reactor was considered.

The following boundary conditions were applied:

- A flat profile was considered for the gas velocity at the gas inlet. The total mass flow rate, and all species' mass fractions were fixed to the experimental values. The inlet gas temperature was set equal to the temperature of the wall close to the inlet.
- A symmetry boundary condition was applied at the YZ symmetry plane.
- A classical no-slip condition was imposed for the gas velocity on the reactor walls, the substrate holder, and the substrates themselves. The temperature of the surfaces was set equal to the temperature profile measured experimentally on the reactor walls before deposition. Due to the steep decrease of the temperature at the exhaust, a constant temperature was applied for the last 100 mm of the reactor; i.e. between 600 and 700 mm, to avoid backflow in the computations and to speed up convergence. Modifying the temperature profile in this region does not impact the results, because samples were placed only between 57 and 500 mm from the reactor inlet. The mass flux density of each species was assumed to be equal to the corresponding heterogeneous reaction rate.
- The reactor exhaust was defined with a pressure-outlet boundary condition. The total pressure was fixed at the operating pressure. A zero diffusion flux was fixed for all gas phase variables.

The chemical reaction rates were implemented into FLUENT® in the form of an Arrhenius type expression:

$$R_r = k_{0,r} \, exp^{\left(-\frac{E_a^r}{RT}\right)} \prod_{i=1}^{i=n} p_i \tag{1}$$

For the surface reaction rates, R_r (kmol m^{-2} s^{-1}) stands for the rate of the reaction r, k_0 (kmol m^{-2} s^{-1} Pa^{-n}) is the pre-exponential factor of the reaction r, $E_a{}^r$ (kJ mol^{-1}) is the activation energy of the reaction r, T (K) is the temperature of the surface where the reaction r occurs, n is the number of involved species, p_i (Pa) is the concentration of the species i. For the homogeneous chemical reactions, R_r is expressed in kmol m^{-3} s^{-1} and $k_{0,r}$ in kmol m^{-3} s^{-1} Pa^{-n}, whereas T (K) is the temperature of the gas phase.

3. Results

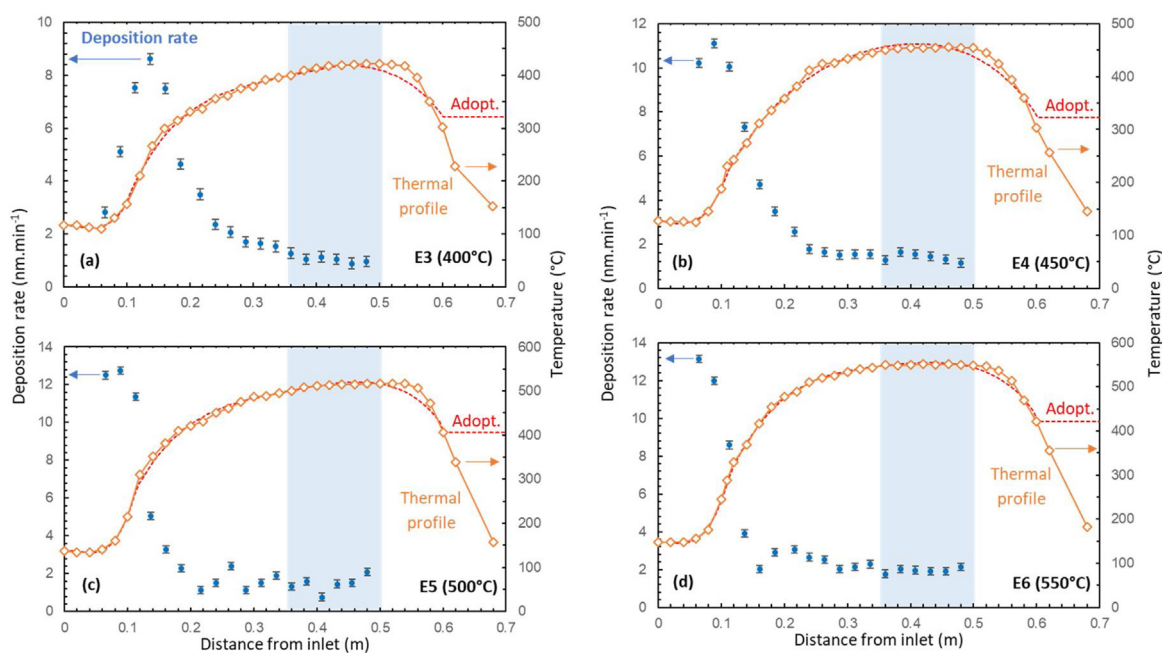### 3.1. Experimental thermal profiles and deposition rates

Fig. 2 shows photographs of the SiO_2 films deposited across the first 12 Si samples placed in the CVD reactor, for the four SP temperatures tested, corresponding to runs E3–E6. The deposition rate on substrates 13–18 was similar to the one on substrate 12. No powder was present on the films. Radial and axial iridescences appear on the surface of the substrates, indicating thickness variations of the films. These variations are directly linked to the chemical mechanisms responsible for the film deposition, as it will be detailed in the forthcoming sections, and are probably enhanced by the thermal gradients existing in the first part of the reactor. The corresponding simulated thickness profiles are also presented in Fig. 2 and will be discussed in Section 3.4.

The thermal profiles and the experimental deposition rates are plotted in Fig. 3 versus the distance from the reactor inlet, for runs E3–E6. For all four runs, the temperature in the first 70 mm of the reactor remains low, i.e. between 115 and 156 °C. After 70 mm, the temperature increases rapidly to reach the target SP temperature at 360 mm. Then, an isothermal zone appears, spanning approximately from 360 to 500 mm.

For run E3, the deposition rate first increases to reach 9 nm min^{-1} until the temperature reaches approximately 250 °C, then decreases in the zone where temperature continuously increases. For runs E4–E6, the deposition rate reaches a maximum value of 11−13 nm min^{-1} at approximately 180 °C, after which it decreases with the temperature, and remains constant within the isothermal region. This behavior could correspond to systems for which at least two different species are responsible for deposition, as it will be discussed in the forthcoming sections.
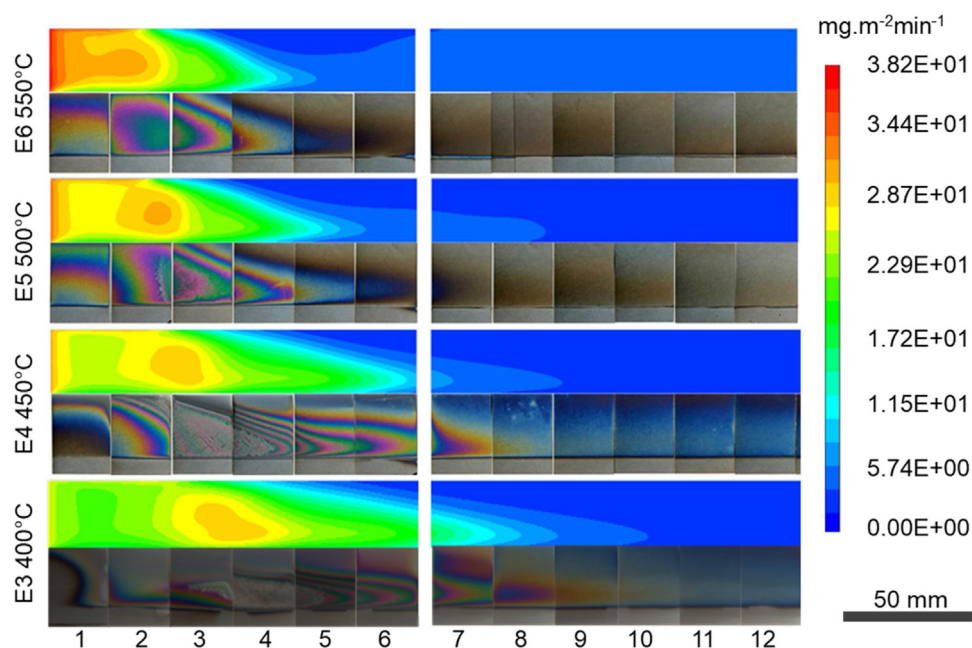
Fig. 2 – Photographs of the SiO₂ films along the substrate holder for runs E3 to E6, and corresponding simulated deposition rate profiles along the YZ plane.
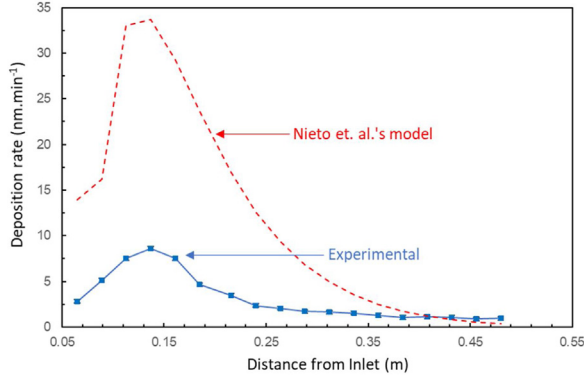

Fig. 3 – Evolution of the experimental deposition rates (blue circles), the reactor's thermal profile (orange diamonds), and the adopted thermal profile (red dashed line), along the reactor length, for runs E3 (a), E4 (b), E5 (c) and E6 (d). Light-blue rectangles depict the considered isothermal regions. (For interpretation of the references to colour in this figure legend, the reader is referred to the web version of this article.)

3.2. Simulation of the deposition rate using existing model

Nieto et al.'s model (Nieto et al., 2005) was used as the starting point for the present work, because, to the best of our knowledge, it is the study closest to the conditions used in our experiments. Their kinetic system (Table S1 in the *Supplementary material*) was implemented into FLUENT® and run E3 was simulated (Fig. 4). A high deposition rate (33 nm min⁻¹) was observed in the first 150 mm of the reactor, due to the intense surface reaction R6 (TEOS + 6O₃ → SiO₂ + O₂ + by-products) between TEOS and O₃. No such deposition rate values were

measured experimentally, as shown in Fig. 3a. This considerable discrepancy can be explained by the fact that Nieto et al. did not consider deposition on the reactor walls, and the average gas temperature of the single-wafer treated in Nieto et al.'s reactor was always about 400 °C, a temperature at which the concentration of O_3 is decreased due to its thermal decomposition through reactions R1 ($O_3 + M \rightarrow O_2 + O + M$), R2 ($O^{\bullet}_3 + O \rightarrow 2O^{\bullet}_2$) and R3 ($2O + M \rightarrow O^{\bullet}_2 + M$). In contrast, the temperature of the first silicon substrate in run E3 does not exceed 150 °C. Because k_6 does not consider any temperature influence in Nieto et al.'s model, their kinetic mechanism is unable to represent our experimental results.

Fig. 4 – Average calculated deposition rates of run E3 (SP 400 °C), simulated using Nieto et al.'s model (red dashed line) and compared to the respective experimental average deposition rates per coupon (blue squares). (For interpretation of the references to colour in this figure legend, the reader is referred to the web version of this article.)

Moreover, this first simulation indicates that the depletion of O_3 impacts the whole model, because of its high reactivity and its quick decomposition with increasing temperature (Reactions (R1)–(R3)) in the first few centimeters of the reactor. For Nieto et al.'s model, INT production (Reaction (R4), O_3+TEOS + M → INT + R + M), depends on the available O_3 in the gas phase, and is only observed at the beginning of the reactor, where O_3 concentration is still sufficient. This must be put in parallel with the underestimation, by Nieto's model, of the experimental deposition rate between 400 mm and the reactor exit, a region where deposition depends on INT contribution. One possible explanation is that the INT concentration is depleted in the gas phase due to its low production by reaction (R4) and high consumption by Reaction (R5), INT→by-products. This indicates that the kinetics of at least Reactions (R4), (R5) and/or (R6) should be modified.

3.3. Development of a new kinetic scheme

According to the previous preliminary experimental observations and computational results, we modified Nieto et al.'s model and kinetic laws based on the following assumptions: (i) the deposition in the vicinity of the inlet region is attributed to the reaction between TEOS and O_3 (R6), exclusively; (ii) the deposition closer to the exhaust, where O_3 is no more present, is attributed to INT.

First, concerning the kinetics of (R6), the experimental results of runs E1–E3 were considered in order to calculate a new partial order exponent a for TEOS. From each run, performed at the same temperature, the first sample from the inlet was selected and its weight gain after deposition was converted into deposition rate. Runs E1–E3 are coupled in pairs of two, and by using the (R6) kinetic law of Table S1 (*Supplementary material*), the ratio of their reaction rates is expressed as:

$$\frac{R6_{E_i}}{R6_{E_j}} = \frac{k_6 [TEOS]_i^a [O_3]_i^{0.25}}{k_6 [TEOS]_j^a [O_3]_j^{0.25}} \tag{2}$$

where $R6$ is the reaction rate of reaction (R6), E_i and E_j are the experimental runs E1, E2, E3, with i = 1–2, j = 2–3, and $i \neq j$. k_6 is the kinetic constant of reaction (R6), $[TEOS]_i$ and $[TEOS]_j$ are the concentrations of TEOS at the inlet for runs E_i and E_j
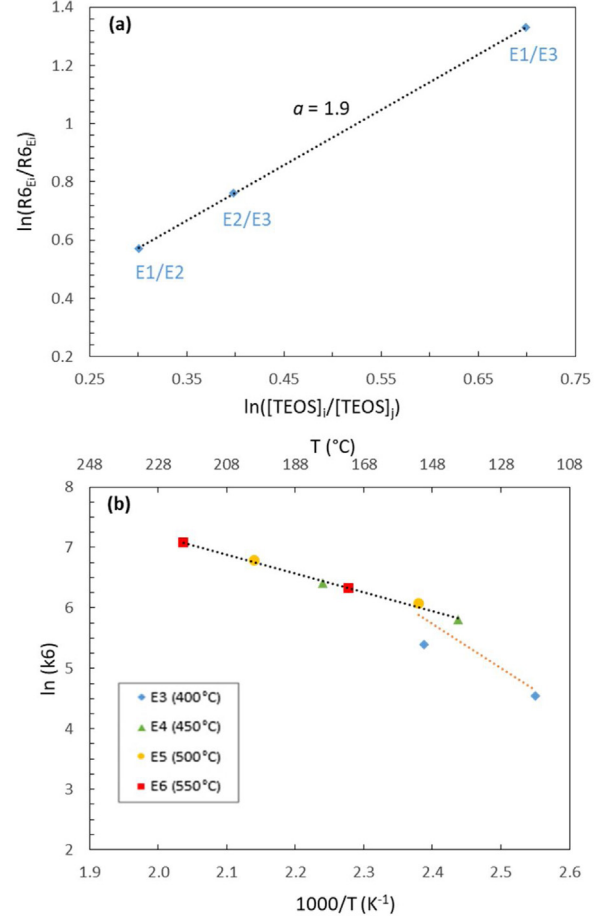
Fig. 5 – (a) Determination of partial order exponent for TEOS in reaction (R6). (b) Linear interpolation of k6 logarithm versus the inverse temperature, plotted for selected samples of runs E3 to E6.

respectively, $[O_3]_i$ and $[O_3]_j$ are the concentrations of O_3 at the inlet for runs E_i and E_j respectively, and a is the partial order exponent of TEOS.

With the kinetic constant k6 remaining unchanged (constant temperature for the considered runs), and assuming that the concentration of O_3 at the inlet is approximately equal across all runs, Eq. (2) is simplified to Eq. (3).

$$\frac{R6_{E_i}}{R6_{E_j}} = \left(\frac{[TEOS]_i}{[TEOS]_j}\right)^a \tag{3}$$

Eq. (3) is then solved for a. The logarithm of $\frac{R6_{E_i}}{R6_{E_j}}$ is plotted versus the logarithm of $\frac{[TEOS]_i}{[TEOS]_j}$ (Fig. 5a). From the slope of Fig. 5a, we deduce a value for a equal to 1.9, with Reaction (R6) now becoming:

$$R6 = k_6 [TEOS]^{1.9} [O_3]^{0.25} \tag{4}$$

This value is higher than the one used by Zhou et al. (a = 1) or Nieto et al. (a = 0.4). The difference may be due to the steep thermal gradient observed in their reactor configurations, which activates the conversion of TEOS to INT through Reaction (R4) more rapidly, downplaying the role of Reaction (R6) and subsequently the influence of the TEOS concentration on the direct SiO_2 deposition.

Our experimental data show a temperature-dependent evolution of the deposition rate in the region where (R6) is

Table 2 – Proposed apparent chemical model, with the respective kinetic laws and constants.				
		Reaction stoichiometry	Reaction rate and kinetic constants	Kinetic constants units
Volumetric reactions(kmol/m³s)	(R1)	$O_3 + M \rightarrow O_2 + O^{\bullet} + M$	$k_1[O_3][M]$ $k_1 = 2.5 \times 10^{11} \times exp\left(-\frac{11430}{T(K)}\right)$	$m^3 kmol^{-1} s^{-1}$
	(R2)	$O_3 + O^{\bullet} \rightarrow 2O_2$	$k_2[O_3][O^{\bullet}]$ $k_2 = 10^{10} \times exp\left(-\frac{2090}{T(K)}\right)$	$m^3 kmol^{-1} s^{-1}$
	(R3)	$2O^{\bullet} + M \rightarrow O_2 + M$	$k_3[O^{\bullet}]^2[M]$ $k_3 = 4 \times 10^8 \times exp\left(+\frac{720}{T(K)}\right)$	$m^6 kmol^{-2} s^{-1}$
	(R4)	$O_3 + TEOS + M \rightarrow INT + R + M$	$k_4[O_3][TEOS][M]$ $k_4 = 4 \times 10^{17} \times exp\left(-\frac{14099}{T(K)}\right)$	$m^6 kmol^{-2} s^{-1}$
Surface reactions(kmol/m²s)	(R6)	$TEOS + 6O_3 \rightarrow SiO_2 + O_2 + \text{by-products}$	$k_6[TEOS]_s^a[O_3]_s^b$ $k_6 = 2.2 \times 10^5 \times exp\left(-\frac{2621.1}{Ts(K)}\right)$ $a = 1.9,\ b = 0.25$	$\frac{kmol_r\, m^{4.45}}{kmol_{TEOS}^{1.9}\, kmol_{O_3}^{0.25}\, s}$
	(R7)	$INT + O_2 \rightarrow SiO_2 + \text{by-products}$	$k_7[INT]_s[O_2]_s$ $k_7 = 1.77 \times exp\left(-\frac{2695.2}{Ts(K)}\right)$	$\frac{kmol_r\, m^4}{kmol_{INT}\, kmol_{O_2}\, s}$
	(R8)	$INT + O_3 \rightarrow SiO_2 + \text{by-products}$	$k_8[INT]_s[O_3]_s$ $k_8 = 2.24 \times 10^7 \times exp\left(-\frac{8345.1}{Ts(K)}\right)$	$\frac{kmol_r\, m^4}{kmol_{INT}\, kmol_{O_3}\, s}$

active. This can be observed in Fig. 3 when comparing the deposition rates of the first sample for each experimental run, a location where the partial pressures of TEOS and O_3 in the gas phase are assumed approximately similar across all runs, the temperature being the only variable. Therefore, the first and second samples closest to the inlet were selected from runs E3–E6, and their respective deposition rate was divided by $[TEOS]_s^{1.9}[O_3]_s^{0.25}$ (by solving Eq. (4) for k_6) and plotted versus the inverse of their local average temperature, spanning from 115 to 230 °C (Fig. 5b). It is worth noting that the two points relative to the lowest SP temperature experiment (run E3) are not aligned with those of the other runs. It is possible that the mechanisms involved at temperatures lower than 150 °C are different than those prevailing between 150 °C and 230 °C. Thus, these two points were not considered. As a consequence, the final model will have a lower accuracy for deposition temperatures lower than 150 °C. The temperature dependent kinetic rate for (R6) was obtained from the results of runs E4–E6, for which an activation energy of 21.8 kJ mol⁻¹ was deduced. It is difficult to comment on this value in relation to literature data, because in this kinetic model, each apparent chemical reaction represents a set of multiple real chemical reactions. Moreover, it is the first time that an activation energy has been calculated for this reaction.

The kinetic law of Nieto's reaction (R7), INT→SiO₂+by-products, was then modified in a similar manner. We assumed that for the conditions tested, INT reacts with an oxygen containing species to form the SiO_2 film. Cleavage of the remaining ethoxy moieties of the intermediate species is facilitated by the reaction of INT with $O^{\bullet}$, O_2, or O_3. The kinetic constants of Reaction (R7) were adjusted based on the experimental results of runs E3–E6, and focused specifically on samples of the isothermal region assumed between 360 to 500 mm. Their deposition rate was divided by the calculated concentration of INT and by that of an oxygen reactive species, then plotted against the inverse of their local average temperature to obtain an Arrhenius plot expression (Fig. S2 of the *Supplementary material*). The two reactive species active in this region for the present configuration and thermal profile are O_2 and $O^{\bullet}$. Unlike Romet et al. (2001) who proposed a deposition mechanism involving the reaction of silanol or diol intermediates with O_3 and $O^{\bullet}$, we used a reaction between INT with O_2 instead, as it represents our experimental results

more accurately. From the above, an activation energy of 22.4 kJ mol⁻¹ was deduced, and Reaction (R7) was reformulated, as detailed in Table 2. Since no decline in the deposition rates was observed close to the exhaust, Reaction (R5) was removed and not applied in our model, similarly to the model of Kim and Gill (1994).

Fig. 6 illustrates the experimental and the computed deposition rates along the length of the reactor, for runs E3–E6. Regions where the simulation overestimates the experimental deposition rates are limited only close to the inlet for runs E3 and E4. In contrast, regions where the simulation underestimates the experimental results are noticeable across all runs, between approximately 70 and 250 mm from the inlet. As such, the respective difference between the two sets of the results is also plotted for each run, for the points where the simulation underestimates the experimental deposition rate. These plots reveal that the agreement between the experimental and the computed deposition rates is not satisfactory. For each run, there is a need for an additional heterogeneous reaction occurring at intermediate temperatures. We assumed that this reaction involves the INT species reacting with oxygen species. By observing the calculated local mass fractions in this specific region, O_3 and $O^{\bullet}$ were considered. Subtracting (R6) and (R7) from the experimental deposition rates, the difference was expressed as either $k_8[INT][O_3]$ or $k_8[INT][O^{\bullet}]$, assuming first order exponents. It was determined that a reaction of INT with O_3 better represents the experimental results. An activation energy of 69.4 kJ mol⁻¹ was deduced for the new heterogeneous Reaction (R8) detailed in Table 2. The addition of multiple surface reactions, where INT is the silicon provider, seems plausible when taking into consideration the wide variety of molecules that INT represents. Romet et al. (2001) mention that the inclusion of additional INT-centered surface reactions improves the model's accuracy and representation of experimental results, something that led them to remove deposition reactions involving TEOS.

The final version of our model and the respective kinetic constants are given in Table 2. It is recalled that all the chemical reactions considered in the model are apparent and stand for numerous elementary mechanisms. Phenomena such as reactive species adsorption, surface diffusion, chemical reaction and product desorption are accounted for in one single surface reaction.
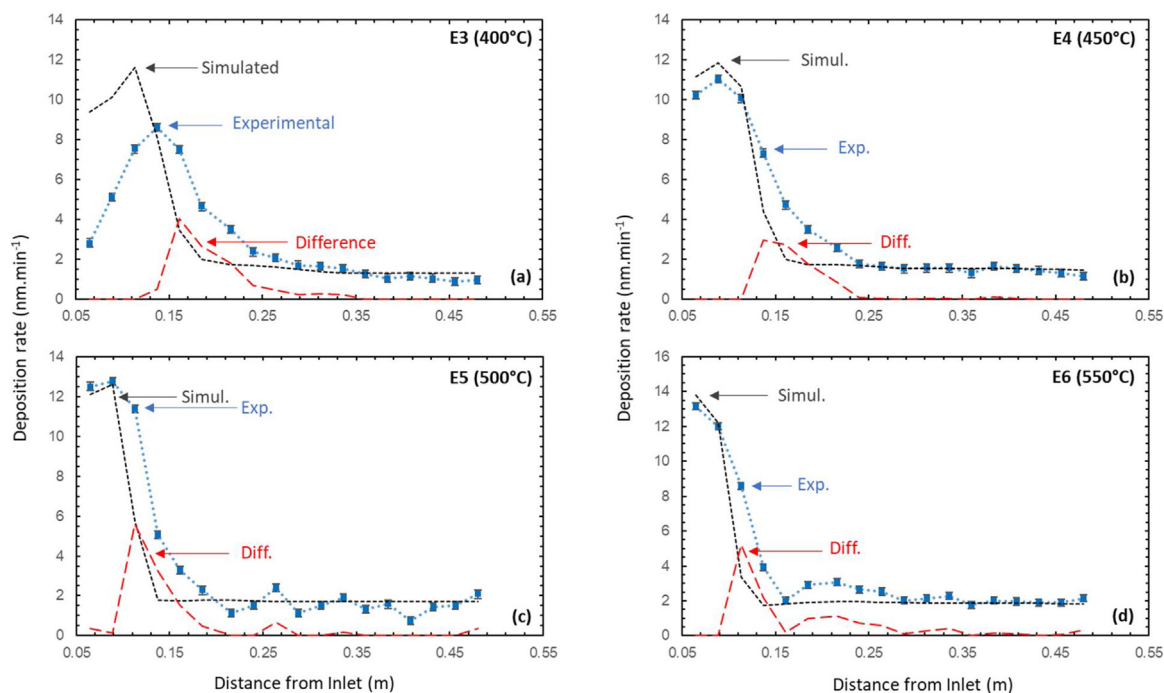
Fig. 6 – Evolution of average experimental deposition rate on each sample (blue squares), average simulated total deposition rate (black dashed line) calculated for each sample, after simulating reactions (R1) to (R7) of the model. Difference of average experimental minus average simulated total deposition rate, for the samples on which the simulation underestimates the experimental rate (red dashed line). (a) Run E3, (b) E4, (c) E5, and (d) E6. (For interpretation of the references to colour in this figure legend, the reader is referred to the web version of this article.)

### 3.4. Validation of the proposed kinetic model

Fig. 7 presents the calculated and experimental deposition rate profiles along the reactor length with the respective TEOS and INT contribution to the film for runs E3 to E6. It appears that the new kinetic model provides very good agreement with the experimental data, with the average relative error of all runs being approximately 17% for the samples located in the isothermal region. The poorest agreement is observed at the inlet zone of run E3 (Fig. 7a) corresponding to the lowest SP temperature, i.e. 400 °C. This is not surprising since we did not consider the inlet zone results of this run to build our model, as explained in Section 3.3. The overestimation of the experimental results in this region further underlines that at a different mechanism possibly takes place for temperatures lower than 150 °C (Fig. 5b).

For runs E4–E6, (Fig. 7b–d), the agreement in the inlet zone is clearly improved with increasing SP temperature. For run E5, i.e. SP 500 °C, experimental errors appear mainly in the isothermal zone due to a slight vertical angular displacement of specific substrates within the substrate holder, causing them to be out of vertical alignment. Lastly, for run E6, i.e. 550 °C (Fig. 7d), a shoulder is observed on the experimental deposition rate data, spanning between 150 and 275 mm, corresponding to a zone where the temperature reaches 520 °C. The model fails to conform to this deposition profile, underestimating the total deposition rate in this region. The existence of this shoulder cannot be attributed to experimental error, such as the vertical, out-of-alignment displacement of the samples, as it is rather uniform in shape and does not appear to be random. It is likely the result of another intermediate reaction contributing to deposition, activated starting from 520 °C, meaning that the model is less accurate above this temperature.

Observing TEOS' and INT's respective contributions to SiO_2 deposition, the simulation results confirm that TEOS is responsible for the formation of the film in the coldest zones close to the inlet of the reactor (first 150 mm of the reactor length) through Reaction (R6). Deposition of SiO_2 from INT through Reactions (R7) and (R8) occurs from around the first 100 mm and until the end of the reactor.

Focusing back on Fig. 2, a visual comparison between photographs of the films and the calculated deposition rate profiles along the substrate holder is shown for runs E3–E6. A remarkable agreement appears on the shape of the profiles, indicating that the main deposition mechanisms are well considered for this operating range. More quantitative, local thickness profiles measured by reflective ellipsometry are compared with simulation in Fig. 8. More specifically, the calculated deposition rate of run E4 was plotted across a horizontal line crossing the substrates' surface (YZ plane), 2 mm below the top edge, to extract CFD simulation results across the exact same line along which the ellipsometry measurements have been acquired.

A remarkable agreement is observed between the calculated and experimental results of Fig. 8, confirming the ability of the model to predict local values of deposition rates. For the first two coupons, the simulations overestimate the local thickness due to the low temperature, as previously explained. Despite that, Fig. 8 is useful for ascertaining that the model can give agreeable local thickness values, complementary to the average deposition rates calculated per coupon in Fig. 7. Lastly, the good agreement in both shape and value thus validates the new chemical and kinetic model as an appropriate simplified representation of the involved chemical mechanisms, for the range of operating conditions tested.
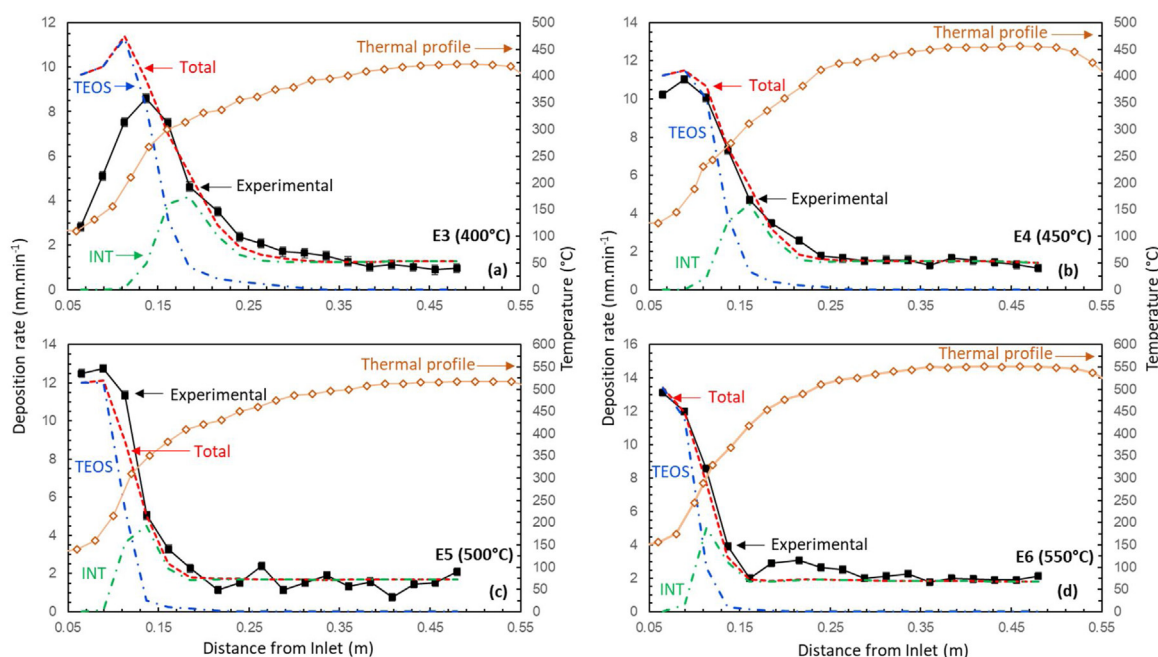
Fig. 7 – Comparison of average experimental deposition rates (black squares) and average total simulated ones (red dashed line) for each coupon of runs E3 (a), E4 (b), E5 (c) and E6 (d). Calculated contributions of TEOS (through reaction (R6)) and INT (through reactions (R7) and (R8)) to deposition are presented by dashed-dotted blue and green lines respectively. Experimental thermal profile (orange diamonds) is included for each run. (For interpretation of the references to colour in this figure legend, the reader is referred to the web version of this article.)
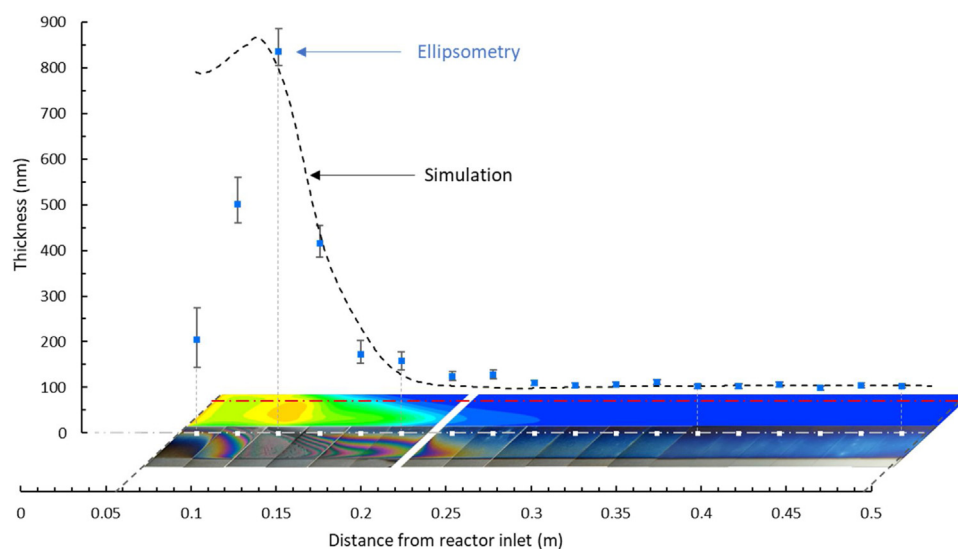

Fig. 8 – Comparison of calculated local thickness (dashed black line) from simulations, and experimental local thickness (blue squares) measured by a refractive ellipsometer for run E4. Photograph of array of samples and scale denoting distance from the reactor inlet are included for visual aid. Red dashed-dotted line represents the line along which the simulation results were extracted. White squares represent the points at which the ellipsometric measurements were taken. (For interpretation of the references to colour in this figure legend, the reader is referred to the web version of this article.)

3.5. Discussion on process simulation results

The validated model provides valuable local hydrodynamic, thermal and mass transfer information for the studied chemical system. Taking run E4 as an example, Fig. 9 presents the local velocity, temperature and mass fraction profiles, whereas Fig. 10 details the local reaction rate profiles. The other runs exhibit similar behavior. All the gas volume profiles are plotted along the XZ horizontal plane crossing the reactor symmetry axis, whereas the surface profiles are plotted on the substrates, along the YZ vertical plane, as illustrated in the top right inset of Fig. 1.

The velocity profile presents a double vortex-like shape in the inlet region and across the first substrates, because the gas is concomitantly heated by the solid surface of the wall and the substrates, and is split in two portions when arriving near the substrates (results detailed in *Supplementary material*). When plotting using the horizontal plane view of Fig. 1, the velocity profile appears parabolic, as classically observed for laminar gas flow. The hottest zones of the reactor logically give rise to the maximum velocity, close to 0.5 m s^{-1}. The corresponding minimum residence time for the gas into the reactor is about 1.4 s. This is a high residence time for a hot wall CVD reactor, and could favor homogeneous chemical reactions,
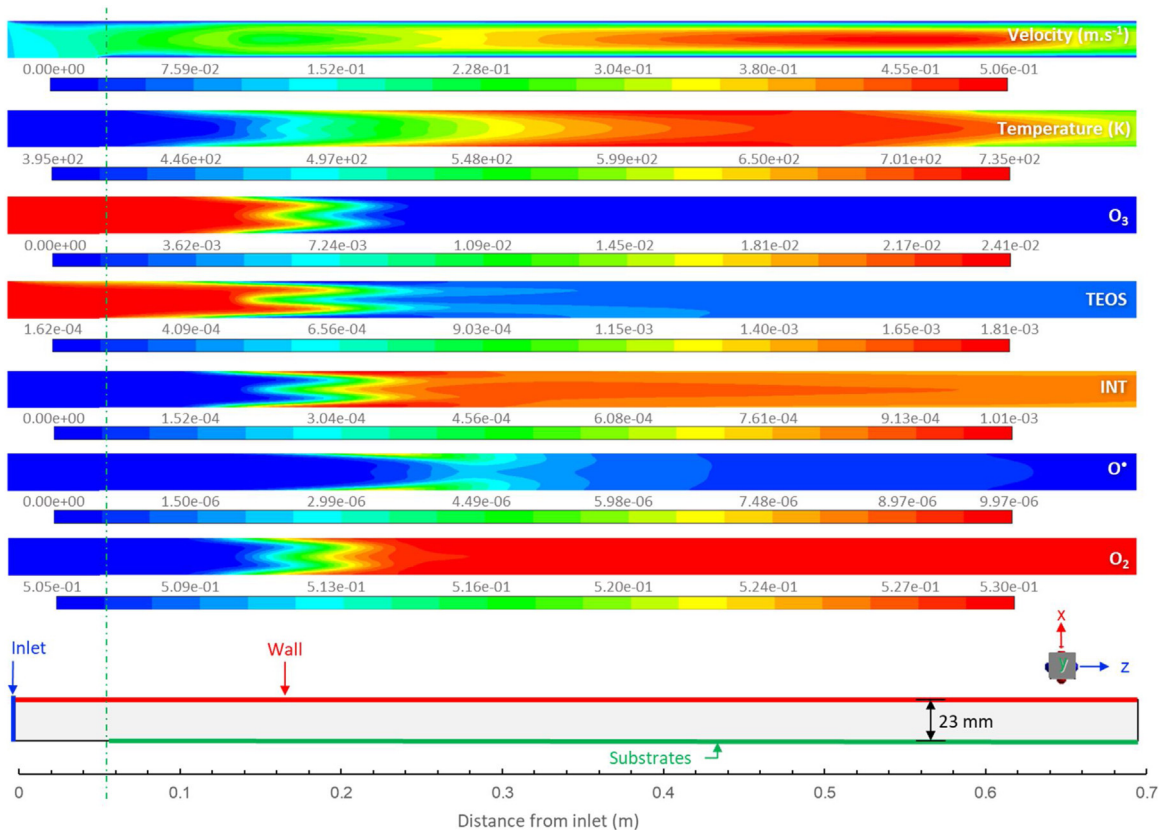
Fig. 9 – Local velocity, temperature and mass fraction profiles of TEOS, INT, O₃, O₂ and O• plotted along the XZ plane for run E4 (450 °C). Vertical green dash-dotted line signifies the start of the substrates at 0.057 m. (For interpretation of the references to colour in this figure legend, the reader is referred to the web version of this article.)
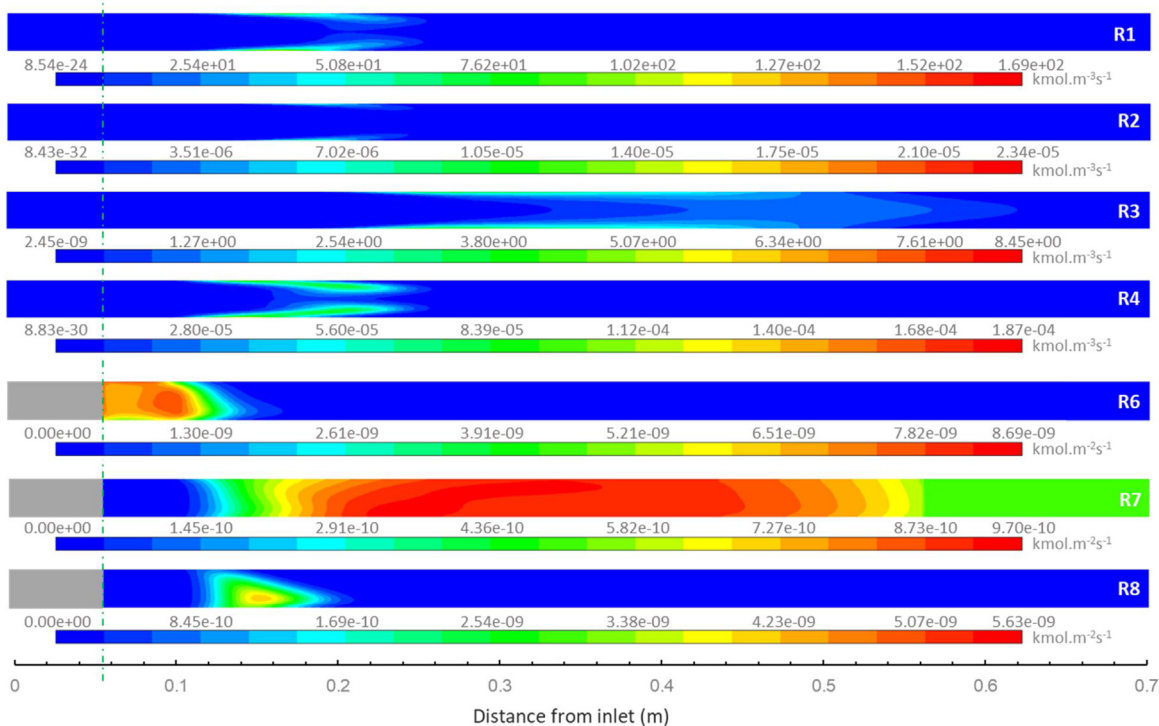
Fig. 10 – Reaction rate profiles for all reactions plotted along the XZ plane for the gas phase reactions ((R1) to (R4)) and along the YZ plane for the surface reactions ((R6) to (R8)) of run E4 (450 °C). Vertical green dash-dotted line signifies the start of the substrates. (For interpretation of the references to colour in this figure legend, the reader is referred to the web version of this article.)

already enhanced by the operation at nearly atmospheric pressure.

The gas temperature remains below 150 °C before the substrates' zone. It then increases and presents a W shape, followed by a parabolic shape in the zone occupied by the substrates. The W shape is due to the two-portion split of the gas previously mentioned and is also observed for the mass fraction profiles as detailed in the *Supplementary material*. The bulk of the gas is logically colder than the gas close to the reactor walls and the substrates. Such profiles can be explained by the dominance of the convective phenomena and by the low thermal conductivity of the gas.

Fig. 9 reveals that the O_3 and TEOS mass fractions remain constant until the average gas temperature reaches a value close to 200 °C at approximately 140 mm from the inlet. From this zone onwards, the TEOS mass fraction decreases due to the heterogeneous Reaction (R6), and then a little further into the reactor, due to the homogeneous (R4) reaction (Fig. 10). O_3 is depleted slightly more rapidly in the same zone, until only a very low mass fraction remains. This depletion is attributed mainly to Reaction (R1), whose kinetics is much higher than all the other homogeneous reactions (Fig. 10), and also to Reactions (R4) and (R8). Reaction (R4) gives rise to the INT species formation in a localized region between approximately 120 and 240 mm from the inlet, after which the reaction rate of (R4) diminishes to very low value, because no more O_3 is present after this zone. For the same reason, Reaction (R8) is also active only in this region, as *a priori* defined. After about 280 mm from the inlet, the TEOS and O_3 mass fractions remain constant, with the O_3 mass fraction being close to zero, and as such Reactions (R4) and (R6) are unable to take place. On the contrary, INT is slowly depleted through reaction (R7), and presents a remarkable 200 mm long zone of uniform value, between 250 and 450 mm from the inlet. Interestingly, despite the mass fractions of INT and O_2 remaining fairly constant after 450 mm, the reaction rate of (R7) decreases, underlining its temperature dependency. The atomic oxygen is formed through reaction (R1) just after the zone corresponding to the concentration decrease of O_3 (between approximately 120 and 220 mm), and appears in low concentrations for most of the reactor's length. For O_2, it is present in excess and thus its mass fraction is uniform inside the reactor, with a slight increase observed in the O_3 depletion zone, mainly due to reaction (R1) and also to Reactions (R2) and (R3).

Overall, the TEOS conversion rate for run E4 is approximately 79%, increasing for higher SP temperatures. Despite that, the global TEOS-to-SiO_2 conversion rate on all solid surfaces remains low does not exceeding 5.2% for all runs. This means that the TEOS conversion involves mainly the gas phase Reaction (R4), which converts TEOS into INT.

The key information is that Reaction (R7) should be favored to uniformly coat complex-in-shape and/or large substrates. In the frame of the development of a new process, the model can be used to optimize both the CVD reactor design and the deposition conditions to enhance this heterogeneous reaction and decrease the other ones.

It is also worth noting the rapid consumption of O_3 even at low temperatures. As a result, TEOS and INT remain unreacted, with Reactions (R4), (R6) and (R8) ending prematurely. In those reactions, O_3 depletion becomes the rate-limiting step, indicating that a higher O_3 flow would be preferable all across the substrate zone. However, increasing the O_3 concentration would lead to higher deposition rates across the whole reactor length in general, and especially at the inlet region where

Reaction (R6) rapidly takes place. As such, big discrepancies in deposition rates between the colder inlet zone and the isothermal region would still exist. An alternative studied was the increase of the total flow rate, as shown in Figure S7 of *Supplementary material*. By increasing the total flow rate up to three times, the deposition profile in the inlet zone is flattened and spread out over a larger region, thus demonstrating the capability of the kinetic model to optimize the deposition process. Nevertheless, the increase of the temperature as the gas progresses towards the isothermal region still leads to the thermal decomposition of O_3 and its depletion in the later parts of the reactor. It becomes apparent that the combined contribution of Reactions (R6) and (R7), along with Reaction (R4), is required for more flat profiles. A proposed solution for higher TEOS-to-INT conversion rate, and TEOS and INT conversion into SiO_2 film to result in higher deposition rates in the isothermal region and an overall flatter deposition profile would be a sequential introduction of ozone at multiple parts along the reactor. For better uniformity, it is proposed to insert O_3 in already heated zones, in order to avoid the abrupt deposition rate due to (R6) in cold zones. This is a known problem, and such a solution has been proposed in other works (Yuan and Mokhtati, 1996; Nieto et al., 2005). Since a multiple injection setup of O_3 cannot be easily implemented experimentally, the present model could be used to help finding the best geometry and operating conditions to increase intermediate conversion and overall yield.

4. Conclusions

The deposition of SiO_2 from a TEOS/O_2/O_3 gas mixture performed by atmospheric pressure CVD is a promising route to provide new surface properties to thermally sensitive substrates. An apparent kinetic model is proposed, in order to represent CVD reactor geometries and deposition conditions able to treat such substrates. The range of validity of the new model is larger in substrate temperature (150–520 °C) and in gas residence time (>0.5 s) than those of the literature.

We applied a methodology combining experimental studies and process analysis by CFD simulation. Experimental results obtained in non-isothermal zones of a hot-wall tubular reactor were simulated using the CFD code FLUENT®.

Based on the model of Nieto et al. (2005), a thermal dependency of the direct formation of SiO_2 from TEOS and O_3 was considered for the first time. For the conditions tested, it was found that the intermediate species resulting from the gas phase decomposition of TEOS participate in two different apparent surface reactions, both producing SiO_2 films. An agreement in shape and value of the calculated local profiles of deposition rates with experimental values validated the new kinetic model.

The analysis of the calculated local evolutions of gas velocity, temperature and species mass fractions provides valuable information about the process behavior. In particular, the detailed contribution of each species to the deposit was discussed and alternative routes of process optimization were proposed. It appears that the model can help in determining the best reactor design and operating conditions to uniformly coat complex and/or large substrates, even at atmospheric pressure. The model could also help in increasing the deposition rate and the TEOS contribution to the deposit by designing a multiple injection system of ozone.

This new model paves the way to develop and optimize new CVD processes allowing to coat a large variety of substrates by SiO_2 thin films at quite low temperatures for innovative applications.

Declaration of interests

The authors declare that they have no known competing financial interests or personal relationships that could have appeared to influence the work reported in this paper.

Acknowledgements

Appendix A. Supplementary data

Supplementary material related to this article can be found, in the online version, at doi:https://doi.org/10.1016/j.cherd.2020.07.007.

References

Adachi, M., Fujimoto, T., Itoh, Y., Okuyama, K., 2000. Numerical simulations of films formed by cluster/particle co-deposition in atmospheric-pressure chemical vapor deposition process using organic silicon vapors and ozone gas. J. Appl. Phys. 39, 3542–3548, http://dx.doi.org/10.1143/JJAP.39.3542.

Arnó, J., 1999. Fourier transform infrared characterization of downstream gas-phase species generated by tetraethylorthosilicate/ozone atmospheric pressure reactions. J. Electrochem. Soc. 146, 276–280, http://dx.doi.org/10.1149/1.1391599.

Azizi, N., Mohammadi, T., Mosayebi Behbahani, R., 2017. Comparison of permeability performance of PEBAX-1074/TiO2, PEBAX-1074/SiO2 and PEBAX-1074/Al2O3 nanocomposite membranes for CO2/CH4 separation. Chem. Eng. Res. Des. 117, 177–189, http://dx.doi.org/10.1016/j.cherd.2016.10.018.

Bird, R.B., Stewart, W.E., Lightfoot, E.N., 2007. Transport Phenomena, second ed. J. Wiley & Sons.

Choi, H.-S., Ryu, C.-H., Hwang, G.-J., 2013. Obtention of ZrO2–SiO2 hydrogen permselective membrane by chemical vapor deposition method. Chem. Eng. J. 232, 302–309, http://dx.doi.org/10.1016/j.cej.2013.07.105.

Coltrin, M.E., Ho, P., Moffat, H.K., Buss, R.J., 2000. Chemical kinetics in chemical vapor deposition: growth of silicon dioxide from tetraethoxysilane (TEOS). Thin Solid Films 365, 251–263, http://dx.doi.org/10.1016/S0040-6090(99)01059-7.

Ding, S.-J., Zhang, D.W., Wang, J.-T., Lee, W.W., 2001. Low dielectric constant SiO2:C,F films prepared from Si(OC2H5)4/C4F8/Ar by plasma-enhanced CVD. Chem. Vap. Depos. 7, 142–146.

Dobkin, D.M., Mokhtari, S., Schmidt, M., Pant, A., 1995. Mechanisms of deposition of SiO2 from TEOS and related organosilicon compounds and ozone. J. Electrochem. Soc. 142, 2332–2340, http://dx.doi.org/10.1149/1.2044296.

Elam, F.M., Starostin, S.A., Meshkova, A.S., van der Velden-Schuermans, B.C.A.M., Bouwstra, J.B., van de Sanden, M.C.M., de Vries, H.W., 2017. Atmospheric pressure roll-to-roll plasma enhanced CVD of high quality silica-like bilayer encapsulation films. Plasma Process. Polym. 14, 1600143, http://dx.doi.org/10.1002/ppap.201600143.

Flores, L.D., Crowell, J.E., 2005. Boundary layer chemistry probed by in situ infrared spectroscopy during SiO2 deposition at atmospheric pressure from tetraethylorthosilicate and ozone. J. Phys. Chem. B 109, 16544–16553, http://dx.doi.org/10.1021/jp0518658.

Fonrodona, M., Escarre, J., Villar, F., Soler, D., Bertormeu, J., Andreu, J., Sabourdji, A., Coulon, N., Mohammed-Brahim, T., 2005. Nanocrystalline top-gate thin film transistors deposited at low temperature by hot-wire CVD on glass. In: Conf. Electron Devices 2005 Span., IEEE, Tarragona, Spain, pp. 183–186, http://dx.doi.org/10.1109/SCED.2005.1504350.

Fujimoto, T., Okuyama, K., Yamada, S., Adachi, M., 1999. Effect of cluster/particle deposition on atmospheric pressure chemical vapor deposition of SiO2 from four gaseous organic Si-containing precursors and ozone. J. Appl. Phys. 85, 4196–4206, http://dx.doi.org/10.1063/1.370331.

Fujino, K., 1993. Step-coverage simulation for tetraethoxysilane and ozone atmospheric pressure chemical vapor deposition. J. Electrochem. Soc. 140, 2309–2312, http://dx.doi.org/10.1149/1.2220814.

Inoue, K., Michimori, M., Okuyama, M., Hamakawa, Y., 1987. Low temperature growth of SiO2 thin film by double-excitation photo-CVD. J. Appl. Phys. 26, 805–811, http://dx.doi.org/10.1143/JJAP.26.805.

Juárez, H., Díaz, T., Pacio, M., García, G., Rosendo, S.E., Rubin, M., Romero, G., García, A., Morales, C., 2007. Optical and electrical characterization of SiO2 films obtained by atmospheric pressure chemical vapor deposition. Phys. Status Solidi C 4, 1481–1484, http://dx.doi.org/10.1002/pssc.200674157.

Kawahara, T., Yuuki, A., Matsui, Y., 1992. Reaction mechanism of chemical vapor deposition using tetraethylorthosilicate and ozone at atmospheric pressure. J. Appl. Phys. 31, 2925–2930, http://dx.doi.org/10.1143/JJAP.31.2925.

Kee, R.J., Dixon-Lewis, G., Warnatz, J., Coltrin, M.E., Miller, J.A., Moffat, H.K., 1998. A Fortran Computer Code Package for the Evaluation of Gas-phase, Multicomponent Transport Properties. The CHEMKIN Collection III, Transport, Reaction Design, San Diego, CA, 42.

Kim, E.J., 1994. Modeling of CVD of silicon dioxide using TEOS and ozone in a single-wafer reactor. J. Electrochem. Soc. 141, 3462–3472, http://dx.doi.org/10.1149/1.2059355.

Kim, E.J., Gill, W.N., 1994. Analytical model for chemical vapor deposition of SiO2 films using tetraethoxysilane and ozone. J. Cryst. Growth 140, 315–326, http://dx.doi.org/10.1016/0022-0248(94)90305-0.

Klaigaew, K., Samart, C., Chaiya, C., Yoneyama, Y., Tsubaki, N., Reubroycharoen, P., 2015. Effect of preparation methods on activation of cobalt catalyst supported on silica fiber for Fischer–Tropsch synthesis. Chem. Eng. J. 278, 166–173, http://dx.doi.org/10.1016/j.cej.2014.11.025.

Kotani, H., Matsuura, M., Fujii, A., Genjou, H., Nagao, S., 1989. Low-temperature APCVD oxide using TEOS-ozone chemistry for multilevel interconnections. In: Int. Tech. Dig. Electron Devices Meet., IEEE, Washington, DC, USA, pp. 669–672, http://dx.doi.org/10.1109/IEDM.1989.74368.

Levin, R.M., 1983. The step coverage of undoped and phosphorus-doped SiO2 glass films. J. Vac. Sci. Technol. B: Microelectron. Nanometer Struct. Process. Meas. Phenom. 1, 54–61, http://dx.doi.org/10.1116/1.582542.

Li, M., Feng, J., Huang, K., Tang, S., Liu, R., Li, H., Ma, F., Meng, X., 2019. Amino group functionalized SiO2@graphene oxide for efficient removal of Cu(II) from aqueous solutions. Chem. Eng. Res. Des. 145, 235–244, http://dx.doi.org/10.1016/j.cherd.2019.03.028.

Liang, H., Han, H., Wang, F., Cheng, Z., Lin, B., Pan, Y., Tan, J., 2019. Experimental investigation on spectral splitting of photovoltaic/thermal hybrid system with two-axis sun tracking based on SiO2/TiO2 interference thin film. Energy Convers. Manag. 188, 230–240, http://dx.doi.org/10.1016/j.enconman.2019.03.060.

Liu, L.-W., Zhou, Q.-W., Zeng, Z.-Q., Jin, M.-L., Zhou, G.-F., Zhan, R.-Z., Chen, H.-J., Gao, X.-S., Lu, X.-B., Senz, S., Zhang, Z., Liu, J.-M., 2016. Induced SERS activity in Ag@SiO2/Ag core-shell

nanosphere arrays with tunable interior insulator: SERS activity in Ag@SiO$_2$/Ag core-shell nanosphere. J. Raman Spectrosc. 47, 1200–1206, http://dx.doi.org/10.1002/jrs.4941.

Liu, L., Yue, Q., Li, G.Q., Xu, K., Wang, J., Wu, Z.Y., Fan, X.A., 2019. Influence of SiO$_2$ insulation layers thickness distribution on magnetic behaviors of Fe-Si@SiO$_2$ soft magnetic composites. J. Phys. Chem. Solids 132, 76–82, http://dx.doi.org/10.1016/j.jpcs.2019.04.016.

Nagel, H., Metz, A., Hezel, R., 2001. Porous SiO$_2$ films prepared by remote plasma enhanced chemical vapour deposition — a novel antireflection coating technology for photovoltaic modules. Sol. Energy Mater. Sol. Cells 65, 71–77, http://dx.doi.org/10.1016/S0927-0248(00)00079-9.

Niéto, J.-P., 2001. Analyse et modélisation d'un réacteur de CVD à fonctionnement continu: Application au dépôt de SiO$_2$ pur et dopé, Ph.D. Dissertation. National Polytechnic Institute of Toulouse, Toulouse, France.

Nieto, J.P., Jeannerot, L., Caussat, B., 2005. Modelling of an industrial moving belt chemical vapour deposition reactor forming SiO$_2$ films. Chem. Eng. Sci. 60, 5331–5340, http://dx.doi.org/10.1016/j.ces.2005.04.079.

Okuyama, K., Fujimoto, T., Hayashi, T., Adachi, M., 1997. Gas-phase nucleation in the tetraethylorthosilicate (TEOS)/O$_3$ APCVD process. AIChE J. 43, 2688–2697, http://dx.doi.org/10.1002/aic.690431313.

Ponton, S., Vergnes, H., Samelor, D., Sadowski, D., Vahlas, C., Caussat, B., 2018. Development of a kinetic model for the moderate temperature chemical vapor deposition of SiO$_2$ films from tetraethyl orthosilicate and oxygen. AIChE J. 64, 3958–3966, http://dx.doi.org/10.1002/aic.16222.

Romet, S., Couturier, M.F., Whidden, T.K., 2001. Modeling of silicon dioxide chemical vapor deposition from tetraethoxysilane and ozone. J. Electrochem. Soc. 148, G82–G90, http://dx.doi.org/10.1149/1.1342186.

Satake, T., Sorita, T., Fujioka, H., Adachi, H., Nakajima, H., 1994. Detection of intermediates in thermal chemical vapor deposition process using tetraethoxysilane. Jpn. J. Appl. Phys. 33, 3339–3342, http://dx.doi.org/10.1143/JJAP.33.3339.

Schoof, G.J., Kleijn, C.R., Van Den Akker, H.E.A., Oosterlaken, T.G.M., Terhorst, H.J.C.M., Huussen, F., 2002. Simulation and validation of SiO$_2$ LPCVD from TEOS in a vertical 300 mm multi-wafer reactor. J. Phys. IV Proc. 12, 51–61, http://dx.doi.org/10.1051/jp4:20020077.

Shareef, I.A., 1995. Subatmospheric chemical vapor deposition ozone/TEOS process for SiO$_2$ trench filling. J. Vac. Sci. Technol. B: Microelectron. Nanometer Struct. Process. Meas. Phenom. 13, 1888–1892, http://dx.doi.org/10.1116/1.587830.

Shareef, I.A., 1996. Role of gas phase reactions in subatmospheric chemical-vapor deposition ozone/TEOS processes for oxide deposition. J. Vac. Sci. Technol. B: Microelectron. Nanometer Struct. Process. Meas. Phenom. 14, 772–774, http://dx.doi.org/10.1116/1.588713.

Sorita, T., Shiga, S., Ikuta, K., Egashira, Y., Komiyama, H., 1993. The formation mechanism and step coverage quality of tetraethylorthosilicate-SiO$_2$ films studied by the micro/macro cavity method. J. Electrochem. Soc. 140, 2952–2959, http://dx.doi.org/10.1149/1.2220938.

Varghese, S., Elfakhri, S., Sheel, D.W., Sheel, P., Bolton, F.J., Foster, H.A., 2013. Novel antibacterial silver-silica surface coatings prepared by chemical vapour deposition for infection control. J. Appl. Microbiol. 115, 1107–1116, http://dx.doi.org/10.1111/jam.12308.

Yuan, Z., Mokhtati, S., 1996. Optimization of SiO$_2$ film conformality in TEOS/O$_3$ APCVD. Thin Solid Films 290–291, 422–426, http://dx.doi.org/10.1016/S0040-6090(96)09018-9.

Zhang, M., Zhang, Z., Liu, Y., Yang, X., Luo, L., Chen, J., Yao, S., 2011. Preparation of core–shell magnetic ion-imprinted polymer for selective extraction of Pb(II) from environmental samples. Chem. Eng. J. 178, 443–450, http://dx.doi.org/10.1016/j.cej.2011.10.035.

Zhang, D.-S., Abadikhah, H., Wang, J.-W., Hao, L.-Y., Xu, X., Agathopoulos, S., 2019. β-SiAlON ceramic membranes modified with SiO$_2$ nanoparticles with high rejection rate in oil-water emulsion separation. Ceram. Int. 45, 4237–4242, http://dx.doi.org/10.1016/j.ceramint.2018.11.095.

Zhou, N., Krishnan, A., Kudriavtsev, V., Brichko, Y., 1997. Numerical study of TEOS/O$_3$ CVD mechanism in an industrial reactor. In: Fifth Int. Conf. on Advanced Thermal Processing of Semiconductors, RTP'97, New Orleans, LA, pp. 257–268.